to Eq. (10), that is, $1 + 0.04\alpha$, does not embody any flow physics and is essentially a curve fit. However, Fig. 2 shows that Eq. (10) adequately predicts the behavior of the wing's a.c. with α, as well as its dependence on sweep. This expression should prove useful for conceptual design studies.

Substituting Eq. (9) into Eq. (5) gives

$$\frac{\Gamma(s)}{Uc(s)} = \frac{[c_s(s)/K]\left(\frac{2}{3} - \text{a.c.}/c\right)}{(1 - k_p k_i)\sin\alpha}$$

which on rearranging and solving for the sectional leading-edge suction (equal to the local vortex lift) becomes

$$c_s(s) = \frac{\Gamma(s)}{Uc(s)} \frac{K(1 - k_p k_i)\sin\alpha}{\left(\frac{2}{3} - \text{a.c.}/c\right)} \tag{11}$$

This expression suggests that the reduction in $\Gamma(s)$ with increasing sweep is counterbalanced by the rearward shift in the wing's a.c. location with increasing sweep. This implies that the relative invariance of vortex lift with increasing Λ is a result of reduced trailing-edge effects such that the net vortex lift coefficient remains relatively constant.

Conclusions

Polhamus's leading-edge suction analogy estimates that the vortex lift coefficient of delta wings is relatively insensitive to wing sweep. This is despite the reduction in vortex strength and increased vortex displacement from the wing surface that results from increasing sweep. An analytical investigation suggests that the invariance of the vortex lift coefficient is a result of increasing slenderness reducing trailing-edge effects. The analysis yields a simple explicit relationship between the a.c. and leading-edge sweep of a delta wing. This in turn allows the prediction of the a.c. and its variance with angle of attack for thin planar delta wings.

Acknowledgment

The author would like to thank Harry Hoeijmakers of the Department of Mechanical Engineering, Twente University, The Netherlands for his helpful comments.

References

[1]Polhamus, E. C., "A Concept of the Vortex Lift of Sharp-Edge Delta Wings Based on a Leading-Edge Suction Analogy," NASA TN D-3767, Oct. 1966.

[2]Traub, L. W., "Prediction of Delta Wing Leading-Edge Vortex Circulation and Lift-Curve Slope," *Journal of Aircraft*, Vol. 34, No. 3, 1997, pp. 450–452.

[3]Hemsch, M. J., and Luckring, J. M., "Connection Between Leading-Edge Sweep, Vortex Lift, and Vortex Strength for Delta Wings," *Journal of Aircraft*, Vol. 27, No. 5, 1990, pp. 473–475.

[4]Visser, K. D., and Nelson, R. C., "Measurements of Circulation and Vorticity in the Leading-Edge Vortex of a Delta Wing," *AIAA Journal*, Vol. 31, No. 1, 1993, pp. 104–111.

[5]Lowson. M. V., "Visualization Measurements of Vortex Flows," *Journal of Aircraft*, Vol. 28, No. 5, 1991, pp. 320–327.

[6]Purvis, J. W., "Analytical Prediction of Vortex Lift," *Journal of Aircraft*, Vol. 18, No. 4, 1981, pp. 225–230.

[7]Roos, F. W., and Kegelman, J. T., "An Experimental Investigation of Sweep-Angle Influence on Delta-Wing Flows," AIAA Paper 90-0383, Jan. 1990.

[8]Kirkpatrick, D. L. I., "Analysis of the Static Pressure Distribution on a Delta Wing in Subsonic Flow," Aeronautical Research Council, Research and Memoranda 3619, London, 1970.

[9]Traub, L. W., "Effects of Spanwise Camber on Delta Wing Aerodynamics: An Experimental and Theoretical Investigation," Ph.D. Dissertation, Aerospace Engineering Dept., Texas A&M Univ., College Station, TX, May 1999.

[10]Lamar, J. E., and Gloss, B. B., "Subsonic Aerodynamic Characteristics of Interacting Lifting Surfaces with Separated Flow Around Sharp Edges Predicted by a Vortex Lattice Method," NASA TN D-7921, Sept. 1975.

Control of a Three-Degree-of-Freedom Airfoil with Limit-Cycle Behavior

Robert L. Clark* and Earl H. Dowell†
Duke University, Durham, North Carolina 27708
and
Kenneth D. Frampton‡
Vanderbilt University, Nashville, Tennessee 37235

Introduction

LIMIT-CYCLE oscillations (LCOs) resulting from control surface freeplay are of concern in many aircraft because they typically occur at a dynamic pressure well below that of the linear flutter boundary. The stability and performance of the aeroservoelastic system is of particular importance in the presence of such nonlinearities that can develop during the life cycle of the aircraft. Results presented by Vipperman et al.[1] served to demonstrate that the control surface actuators can be used to provide successfully gust alleviation and extend the flutter boundary for a three-degree-of-freedom, linear, aeroelastic model. Additionally, Vipperman et al.,[2] as well as Frampton and Clark,[3] demonstrated that robust control strategies can be applied in the design of compensators for a family of dynamic pressures.

The purpose of this work is to investigate the effect of control surface freeplay nonlinearities on the closed-loop performance of a three-degree-of-freedom aeroelastic system. In particular, control systems designed for an open-loop linear three-degree-of-freedom system were applied to a nonlinear three-degree-of-freedom system and evaluated for their performance. It is vital that these linear compensators display stable, closed-loop response in the presence of freeplay nonlinearities that may evolve over the life cycle of the aircraft. Results from this study indicate that the limit-cycle amplitudes in both pitch and plunge can be attenuated significantly through the application of controllers designed for a linear three-degree-of-freedom aeroelastic system. The primary mechanism of control serves to convert high-amplitude, low-frequency LCOs to low-amplitude, high-frequency LCOs for the case considered.

In previous work the dynamic response of a three-degree-of-freedom aeroelastic typical section model with a single control surface extending over the span of the airfoil was investigated both analytically and experimentally.[4] In particular, control surface freeplay was investigated, and LCOs were observed. The freeplay nonlinearity was designed to produce a piecewise linear change in the structural stiffness of the control surface,[4] and the three-degree-of-freedom model was subjected to two-dimensional, incompressible flow. The development of the aeroelastic system follows that of Edwards et al.[5]

Three-Degree-of-Freedom System Model Description

As detailed by Conner et al.,[4] the three-degree-of-freedom model here is based upon the state-space model originally proposed by Edwards et al.[5] A schematic diagram of the model is depicted in Fig. 1. As illustrated, a flap control surface is attached to the wing, and a spring C_β provides a restoring force to the neutral position. The structural nonlinearity introduced for the purpose of this analysis is a spring with a symmetric freeplay region.

A block diagram of the dynamic system model is presented in Fig. 2. As illustrated, a structural nonlinearity is included in the

Received 20 May 1998; revision received 20 October 1999; accepted for publication 24 January 2000.

*Associate Professor of Mechanical Engineering and Materials Science, Box 90300.

†J.A. Jones Professor of Mechanical Engineering and Material Science, Box 90300.

‡Assistant Professor of Mechanical Engineering, Box 1592 Station B.

feedback element associated with the flap stiffness. The freeplay nonlinearity, as detailed by Conner et al.,[4] produces a piecewise linear change in the structural stiffness associated with the flap restoring stiffness. In addition to the dynamics of the nonlinear aeroelastic system, the dynamics of the actuator used to control the surface were modeled as detailed by Vipperman et al.[1] The mechanical properties of the actuator (mass and damping) are added to that of the flap while the first-order electrical dynamics can be cast in state variable form as follows:

$$\left(\frac{\mathrm{d}I(t)}{\mathrm{d}t}\right) = \left(-\frac{R_{\mathrm{act}}}{L_{\mathrm{act}}}\right)\{I(t)\} + \begin{pmatrix} \dfrac{-Blx_{\mathrm{act}}}{L_{\mathrm{act}}} & \dfrac{Blx_{\mathrm{act}}}{L_{\mathrm{act}}} & \dfrac{1}{L_{\mathrm{act}}} \end{pmatrix} \begin{Bmatrix} \dot{\beta}(t) \\ \dot{\alpha}(t) \\ v(t) \end{Bmatrix} \tag{1}$$

where $I(t)$ is the current in the actuator, R_{act} and L_{act} are the coil resistance and inductance, Bl is the electromechanical constant, x_{act} is the actuator moment arm, and $v(t)$ is the applied voltage. The actuator output equation creates the actuator force as follows:

$$\{F_{\mathrm{act}}\} = [Bl]\{I(t)\} \tag{2}$$

The parameters describing the geometry of the typical section are identical to those presented by Conner et al. with a few differences.[4]

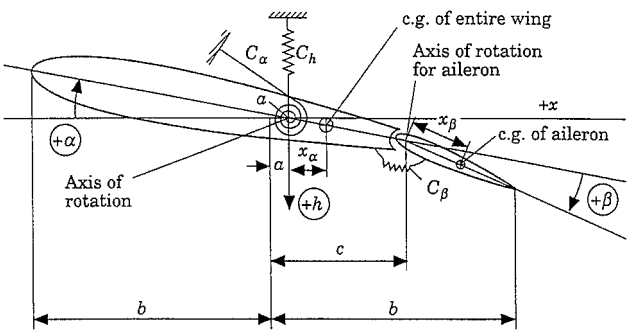

Fig. 1 Schematic of three-degree-of-freedom model (after Conner et al.[4]).

The primary difference is caused by the additional mass and damping of the actuator.

Control System Design

The block diagram of the model presented in Fig. 3 was used to synthesize the controllers for the purpose of this work. The controllers were designed assuming a linear stiffness element (i.e., the nonlinear element in the block diagram of Fig. 2 was replaced with a linear stiffness element). $\mathcal{H}_2$-synthesis was used to design controllers at each flow speed presented. In previous work by Vipperman et al.,[2] dynamic compensators were synthesized to operate over the entire flow regime; however, for the purpose of this study, the objective was to determine the limits of performance at each flow speed.

Both process noise and sensor noise were used as disturbance inputs, and the cost function was constructed from the square of the 2-norm between the error z and the disturbance w. The cost function can be expressed mathematically as follows:

$$J = \lim_{t \to \infty} \{E[z^T(t)z(t)]\} = \|T_{zw}\|_2^2 \tag{3}$$

where T_{zw} is the closed-loop transfer function between z and w. For the purpose of this work, the disturbance w was composed of both process noise and sensor noise, as is typical of linear quadratic

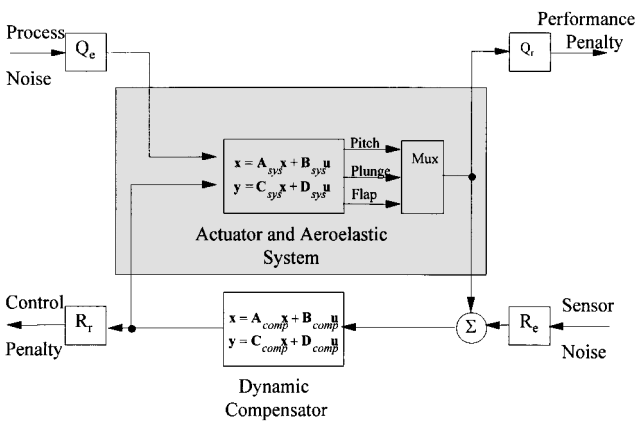

Fig. 3 Block diagram of control system design model.

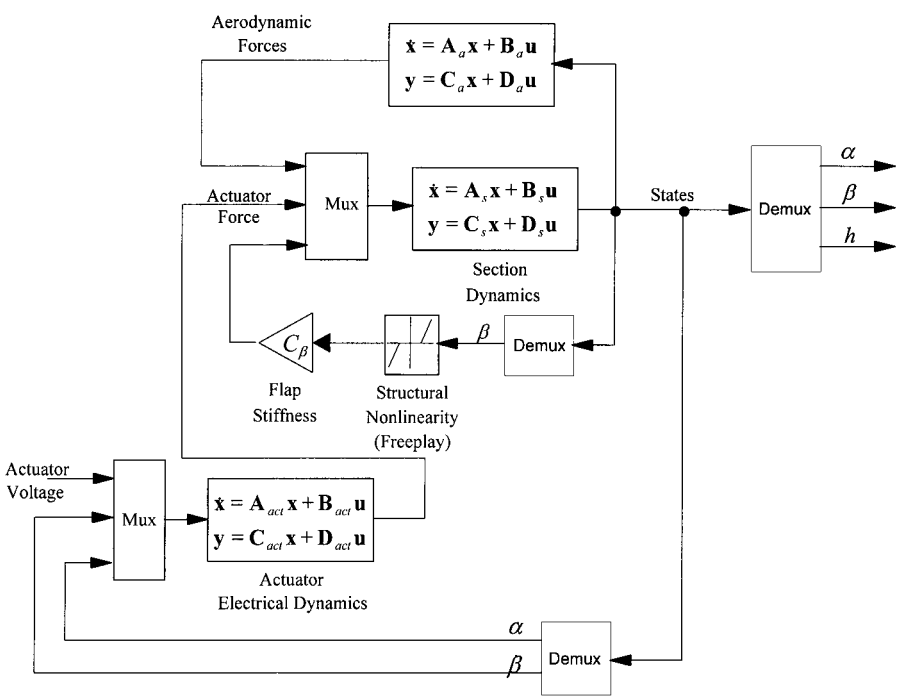

Fig. 2 Block diagram of three-degree-of-freedom model with freeplay nonlinearity in flap restoring spring.

Gaussian design. The error outputs z were constructed from a scalar weighting of the response in pitch, plunge, and flap position as well as a control effort as follows:

$$z = \begin{bmatrix} Q_r^{\frac{1}{2}} & 0 \\ 0 & R_r^{\frac{1}{2}} \end{bmatrix} \begin{Bmatrix} y \\ u \end{Bmatrix} \tag{4}$$

where R_r is a scalar; y is a vector containing the pitch, plunge and flap sensor voltages; and u is the control actuator input voltage. The weighting matrix Q_r is defined as

$$Q_r = \begin{bmatrix} q_{\text{pitch}} & 0 & 0 \\ 0 & q_{\text{plunge}} & 0 \\ 0 & 0 & q_{\text{flap}} \end{bmatrix} = \begin{bmatrix} 1 & 0 & 0 \\ 0 & 5 & 0 \\ 0 & 0 & 1 \end{bmatrix} \tag{5}$$

Two alternative design procedures were considered. In the first design alternative the scalar weighting on flap position q_{flap} was set to zero in the error outputs. The flap position was thus not considered as part of the cost function for the first test case. However, in the second test case the flap position was included in the cost function. For case 1, $q_{\text{pitch}} = 1$, $q_{\text{plunge}} = 1$, $q_{\text{flap}} = 0$, and $R_r = 10^{-10}$. For case 2, $q_{\text{pitch}} = 1$, $q_{\text{plunge}} = 1$, $q_{\text{flap}} = 0.1$, and $R_r = 10^{-10}$. These design parameters were fixed over all flow speeds investigated. For all cases pitch, plunge, and flap were used as outputs to generate the single control signal, which was applied to the moving coil actuator.

Results

The controllers were designed for the linear system with no freeplay in the restoring torque applied to the flap. Controllers were designed with penalties on response in pitch, plunge, and control effort. Additionally for comparison, the flap response was included in one cost function and not in the other as detailed in the preceding section. The synthesized controllers were then applied to the nonlinear model including the freeplay. The objective was to quantify the effect of freeplay on closed-loop performance and also the effect of the dynamic compensator on the closed-loop nonlinear system.

Before considering the response at specific flow speeds, it is instructive to review the results obtained from all flow speeds concurrently. Consider the results presented in Fig. 4. As illustrated, the nondimensional rms LCO recorded in pitch, plunge, and flap response are presented as a function of nondimensional flow speed. The rms amplitudes of pitch and flap response are normalized with respect to the freeplay (±2 deg). The rms amplitude of plunge response is normalized with respect to the product of freeplay and chord length (0.254 m), and the flow speed is normalized with respect to the flutter speed for the open-loop, linear system ($U_f = 23.6$ m/s). The dominant frequency associated with the flap LCO is also plotted as a function of nondimensional flow speed for each case. The open-loop response of the nonlinear system is presented to provide a basis for comparison. Closed-loop responses based upon compensators designed from the two different cost functions are compared. As detailed by Conner et al.,[4] the open-loop, limit-cycle behavior displays two distinct regions of response as a function of flow speed.

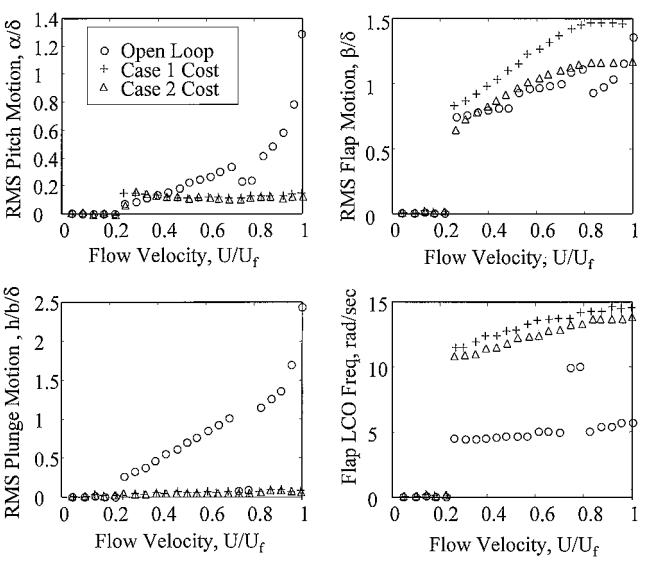

Fig. 4 Plots of nondimensional rms amplitude of LCO in pitch, plunge, and flap response as well as fundamental flap LCO frequency as a function of nondimensional flow speed.

As illustrated, at low nondimensional flow speed $0.2 \leq U/U_f \leq 0.75$, the rms open-loop response for pitch and plunge is characterized by a high-amplitude response, and the LCO frequency of the flap is low (5 Hz). However, for $0.75 < U/U_f \leq 0.85$ the open-loop response in plunge is characterized by low-amplitude LCO, and the flap is characterized by high-frequency LCO, approximately 10 Hz for the example provided. For $0.75 < U/U_f < 0.85$ the rms amplitude associated with plunge drops dramatically, by an order of magnitude compared with the rms response observed at $U/U_f < 0.75$. The decrease in rms amplitude associated with pitch is less dramatic and regains its amplitude at $U/U_f > 0.85$. In general, a significant region of transition is observed in the aeroelastic response, as was detailed by Conner et al.[4] However, with the added inertia of the moving coil actuator and the added dynamics resulting from the electromechanical coupling of the transducer, some deviations in characteristic response are expected.

When the responses to pitch, plunge, and control effort were used in the cost function, the rms amplitude of the LCO in pitch and plunge was decreased dramatically. In fact, upon considering the fundamental flap LCO frequency, one observes that the closed-loop response is characterized by a higher-frequency, lower-amplitude, LCO over the entire nondimensional flow regime, which was expected because the servo-controlled flap results in a higher closed-loop bandwidth. To the detriment of the compensator designed from this cost function, the flap response increases significantly above that of the open-loop response for $U/U_f > 0.4$. The LCO is essentially transferred from the plunge response to the flap response, as in a tuned vibration absorber.

Upon including flap position in the cost function, the closed-loop response of the nonlinear system was modified. As illustrated in Fig. 4, the rms amplitude corresponding to the flap LCO was maintained on the order of that measured under open-loop conditions for $0.2 < U/U_f < 0.75$. The rms amplitude corresponding to the pitch and plunge LCO was reduced significantly, on the same order of magnitude as that achieved with the compensator resulting from the preceding design case. Additionally, the closed-loop response of the nonlinear system is characterized by a high-frequency flap LCO. Again, this high-frequency LCO in flap response results from the extended bandwidth of the closed-loop system.

In both closed-loop control cases the LCO associated with pitch and plunge was affected in a positive manner, reducing the rms amplitudes. However, to adequately constrain the flap response, one must also include a penalty on flap response in the cost function. Integrating this penalty into the cost function resulted in reduced rms LCO response associated with pitch, plunge, and flap displacement over all nondimensional flow speeds. The primary benefit of this added performance variable was observed in the reduction of rms flap response. The open-loop LCO of the flap is dominated by a frequency very close to that associated with the plunge resonance. However, the closed-loop LCO of the flap is dominated by a frequency very close to that associated with the flap resonance.

Conclusions

The purpose of this work was to investigate the effect of a flap stiffness freeplay nonlinearity on the closed-loop stability and performance of a three-degree-of-freedom aeroelastic system. Results from this study demonstrate that controllers designed for the linear system with flap restoring force serve to reduce the LCOs associated with pitch and plunge while maintaining the same level of LCO in the flap response as long as the flap response is included as a performance variable in the design of the compensator. The flap LCO frequency for the open-loop nonlinear system is dominated by

a frequency corresponding to the plunge resonance. For the closed-loop, nonlinear system, the dominant LCO frequency is approximately that of the flap resonance. The primary effect of the dynamic compensator serves to convert the high-amplitude, low-frequency LCOs of the nonlinear system to low-amplitude, high-frequency LCOs.

Acknowledgment

The authors gratefully acknowledge the Air Force Office of Scientific Research for funding this research under Grant F49620-96-1-0385, monitored by Maj. Brian Sanders.

References

[1]Vipperman, J. S., Clark, R. L., Conner, M., and Dowell, E. H., "Investigation of the Experimental Active Control of a Typical Section Airfoil Using a Trailing Edge Flap," *Journal of Aircraft*, Vol. 35, No. 2, 1998, pp. 224–229.

[2]Vipperman, J. S., Barker, J. M., Clark, R. L., and Balas, G. J., "Comparison of μ- and $\mathcal{H}_2$-Synthesis Controllers on an Experimental Typical Section," *Journal of Guidance, Control, and Dynamics*, Vol. 22, No. 2, 1999, pp. 278–285.

[3]Frampton, K. D., and Clark, R. L. , "Experiments on Control of Limit Cycle Oscillations in a Typical Section," *Journal of Guidance, Control, and Dynamics* (to be published).

[4]Conner, M. D., Tang, D. M., Dowell, E. H., and Virgin, L. N., "Nonlinear Behavior of a Typical Airfoil Section with Control Surface Freeplay: A Numerical and Experimental Study," *Journal of Fluids and Structures*, Vol. 11, No. 1, 1997, pp. 89–109.

[5]Edwards, J. W., Ashley, H., and Breakwell, J. V., "Unsteady Aerodynamic Modeling for Arbitrary Motions," *AIAA Journal*, Vol. 17, No. 4, 1979, pp. 365–374.

Modification of a Helicopter Inverse Simulation to Include an Enhanced Rotor Model

Sharon A. Doyle* and Douglas G. Thomson†
Glasgow University,
Glasgow, Scotland G12 8QQ, United Kingdom

Nomenclature

h	= maximum maneuver height, m
I_R	= effective inertia of the main rotor, kg · m^2
K_3	= engine model gain
k	= current solution time point
n_{pts}	= number of points in inverse simulation/maneuver
Q_E	= engine torque, N · m
Q_R	= main rotor torque, N · m
Q_{TR}	= tail rotor torque, N · m
Q_{tr}	= transmission torque, N · m
r	= fuselage yaw rate, rad/s
t	= time, s
t_k	= time point in inverse simulation/maneuver definition
t_m	= time taken to complete a maneuver, s
$\boldsymbol{u}$	= control vector
V_f	= aircraft flight velocity, m/s
x_e, y_e, z_e	= displacements relative to an Earth-fixed inertial frame, m
$\boldsymbol{y}$	= output vector
$\boldsymbol{y}_{\text{des}}$	= desired output vector
Δt	= inverse simulation/maneuver discretization interval, s
θ_0	= main rotor collective pitch angle, rad
$\theta_{0\text{tr}}$	= tail rotor collective pitch angle, rad
θ_{1s}, θ_{1c}	= main rotor longitudinal and lateral cyclic pitch angles, rad
τ_{e1}, τ_{e2}, τ_{e3}	= engine time constants, s
ψ	= heading, rad
ψ_{azi}	= blade azimuth angle, rad
Ω	= main rotorspeed, rad/s
Ω_i	= idling rotorspeed, rad/s

Received 26 March 1999; revision received 21 September 1999; accepted for publication 21 September 1999.

*Postgraduate Research Student, Department of Aerospace Engineering, James Watt Building.

†Senior Lecturer, Department of Aerospace Engineering, James Watt Building.

I. Introduction

AN individual blade rotor model has been developed at the University of Glasgow by Rutherford and Thomson[1] for use in helicopter inverse simulation. In the context of helicopter flight dynamics, an inverse simulation generates the control time histories for the modeled helicopter performing a defined task. To implement such a model in an inverse sense, it is necessary to adopt a numerical integration technique similar to that proposed by Hess et al.[2] The generic inverse simulation algorithm (Genisa) used by Rutherford and Thomson is described in detail in Ref. 1, where the problem of numerical stability is also addressed.

The helicopter individual blade rotor model (Hibrom) represents the state of the art in helicopter inverse simulation. Some simplifying assumptions were made in its development; the most significant of which is the assumption of constant rotorspeed (see Ref. 1; Conclusions). It is important to model this degree of freedom because it has a direct influence on the dynamic behavior of the main rotor. In addition, the inclusion of the rotorspeed degree of freedom must be achieved before other modeling features, such as lead/lag freedom, can be incorporated. This Engineering Note describes modifications made to the inverse algorithm Genisa that allow the rotorspeed degree of freedom to be incorporated within Hibrom.

II. Genisa

The integration-based inverse solver Genisa is essentially a modification of that documented by Hess et al.[2] and is driven by specified maneuver constraints. The starting point is, therefore, a mathematical definition of the desired flight path to be followed by the subject vehicle. Genisa operates by constraining the helicopter's Earth-referenced accelerations along with one attitude (heading in the case of a longitudinal maneuver), and so the desired output vector $\boldsymbol{y}_{\text{des}}$ is evaluated for a series of n_{pts} discrete time points:

$$\boldsymbol{y}_{\text{des}}(t_k) = \{\ddot{x}_e(t_k) \quad \ddot{y}_e(t_k) \quad \ddot{z}_e(t_k) \quad \dot{\psi}(t_k)\}^T$$

$$0 \le t_k \le t_m, \quad k = 1, n_{\text{pts}} \qquad (1)$$

The altitude $z_e(t_k)$ is specified as a polynomial function of time.

The Genisa algorithm then proceeds by making an initial estimate of the applied control inputs that, over a predefined time increment, will result in the helicopter having the desired accelerations and heading. These control displacements are applied to the helicopter model, and the equations of motion are solved by numerical integration to obtain the helicopter's actual states at the next time point. An iterative scheme is then set up whereby control displacements are adjusted until the error between desired and actual outputs is within a prescribed tolerance. This process is repeated for each time interval, yielding a control time history $\boldsymbol{u}(t_k)$ for the complete maneuver, where

$$\boldsymbol{u}(t_k) = \{\theta_0(t_k) \quad \theta_{1s}(t_k) \quad \theta_{1c}(t_k) \quad \theta_{0\text{tr}}(t_k)\}^T \qquad (2)$$

The success of the method just outlined relies on the selection of a suitable time step Δt, over which the applied controls are to be held constant. The rotor forces and moments are calculated by integrating elemental forces over the span of each blade. Because the velocity at each spanwise location varies as the blade rotates, the total force calculated is harmonic with period equal to a complete revolution of the blade (or $1/n$ revolutions of an n-bladed rotor). For